UCSF

UC San Francisco Electronic Theses and Dissertations

Title

Tissue Segmentation and Classification for PET/MR MR-based Attenuation Correction Using Zero-echo Time (ZTE) MRI

Permalink

https://escholarship.org/uc/item/96q3t19t

Author

Leynes, Andrew

Publication Date

2015

Peer reviewed|Thesis/dissertation

Tissue Segmentation and Classification for PET/MR MR-based
Attenuation Correction Using Zero-echo Time (ZTE) MRI

by

Andrew Leynes

THESIS

Submitted in partial satisfaction of the requirements for the degree of

MASTER OF SCIENCE

in

Biomedical Imaging

in the

GRADUATE DIVISION

of the

UNIVERSITY OF CALIFORNIA, SAN FRANCISCO

Dedication and Acknowledgements

I dedicate this thesis to my family. Without all their support, I would not have had the opportunities presented to me. For all the blessings and encouragement that I receive from them everyday, I am thankful.

I would like to thank Dr. Peder Larson. At the very beginning of this Master's program, he excellently taught us the fundamentals of Magnetic Resonance Imaging, and started my path towards this thesis. His constant presence, availability, guidance, and support are top notch, and I am very thankful to have him as my thesis adviser.

To Dr. Julio Carballido-Gamio and Dr. Jaewon Yang, for providing much needed input and guidance in my thesis, and for being patient with me and making yourselves available to answer my questions: thank you!

To my classmates: Jay, Jeff, Omar, Tiff, Sam, Joe, Liz, and Liz, Solomon, Sonia, Terry, Nate, Divya, Kai, Hecong, and Gina. Thanks for the amazing year. I wish you all the best!

Dr. David Saloner, Dr. Alastair Martin, Robert Smith, Melinda Parangan-Chu, the MSBI faculty and administration, thank you for giving us this opportunity. Thank you for teaching us, and supporting us throughout the entire year.

This paper was typeset in LATEX.

Tissue Segmentation and Classification for PET/MR MR-based Attenuation Correction Using Zero-Echo Time (ZTE) MRI

ANDREW LEYNES

Abstract

To reduce errors in the reconstructed PET image, the photon attenuation of all tissues needs to be accounted for. Current sequence-based methods to generate an MR-derived attenuation map are unable to account for all tissue classes. Recent work has demonstrated that there is phase contrast in ultrashort echo time (UTE) or zero echo time (ZTE) images that would allow classification of all necessary tissue classes (bone, air, fat, and water) from only a single ZTE scan. The aim of this thesis is to demonstrate the feasibility of generating a pseudo-CT attenuation map based on bone, air, fat, and water classifications from a single ZTE acquisition. A 3D image of the pelvis was acquired using a ZTE pulse sequence on a 3T GE Signa PET/MRI system. Semi-automated algorithms were used to segment bone, air, and soft tissue from the ZTE magnitude image. Air was segmented using an intensity limited region growing algorithm and global thresholding. Bone was segmented by enhancing bone, and then using global thresholding. Soft tissue was defined as regions where bone and air were absent. A continuous-value fat/water map was then generated with fuzzy c-means clustering using the ZTE phase image and the soft tissue mask. Appropriate HU values were assigned to the segmented tissue maps, and combined to produce the pseudo-CT attenuation map. Qualitative comparisons with CT, and Dixon pseudo-CT images presented similar tissue classification results. Preliminary results demonstrate that bone, air, fat, and water can be classified using a single ZTE acquisition.

iv

Contents

List of Tables

List of Figures

1   Introduction

Multi-modality imaging is becoming the standard of clinical care. It allows one to gain more information by simultaneously analyzing data provided by different imaging modalities. Each modality provides different information. Computed Tomography (CT) mainly provides structural and anatomic information, and can provide functional information using contrast agents. Positron Emission Tomography (PET) or Single Photon Emission Tomography (SPECT) gives excellent functional information. Magnetic Resonance Imaging (MRI) can give structural, anatomic, metabolic, or functional information with unparalleled soft-tissue contrast.

By combining the images from different modalities, more information can be gained. Figure 1 shows the use of PET/MRI. By combining the two modalities, it was discovered that the patient had a glioma in two different locations. If only a single imaging modality was used, only a single tumor would have been detected.
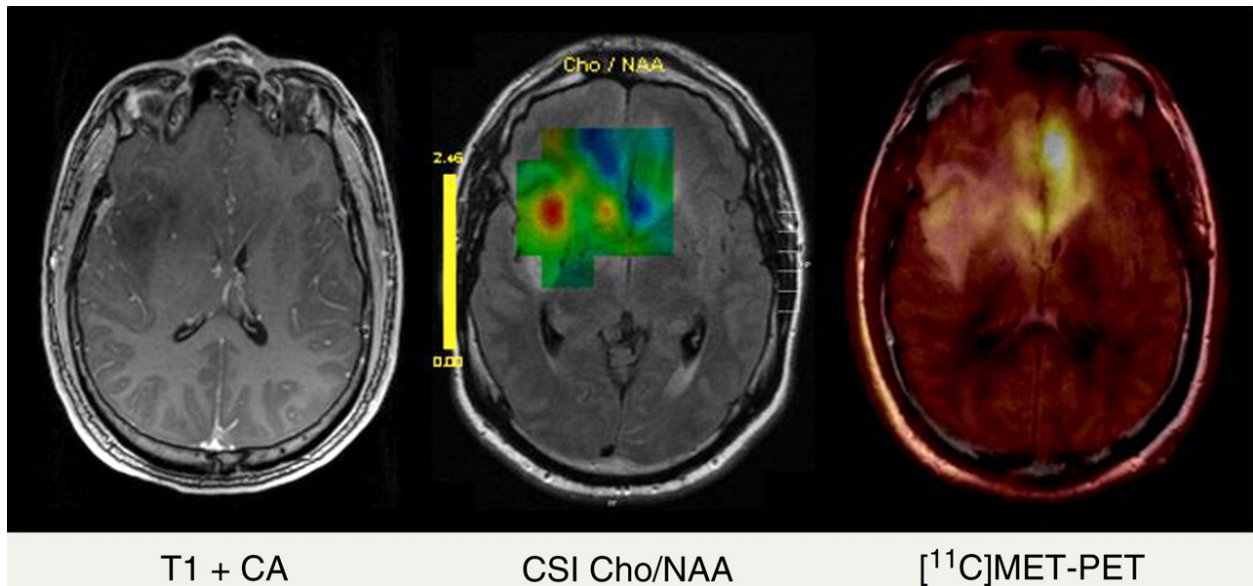
Figure 1: Multi-modality imaging of the brain.
An image of the brain with standard contrast-enhanced T1-weighting (left), chemical shift imaging (CSI) (center), and 11C-methionine PET/MRI (right).[1] Standard T1-w MRI displayed some contrast enhancement. CSI mapping showed a hot spot in the right insular region while 11C-methionine uptake was mostly in the basal frontal lobe on the left side. Because of the discrepancy between CSI and the PET, biopsy was done in both locations and found anaplastic glioma in the frontal left region and low-grade glioma in the right insular region.

Another example is shown in Figure 2. Liver metastases were not apparent on the CT nor PET images, however they were visible on the liver MRI. Compared to MRI, CT has lower soft tissue contrast, and the 18F-FDG has physiologically low liver uptake. The use of multiple modalities compensates for the weakness of each modality in order to give a reliable diagnosis.

Figure 2: Multi-modality imaging of the liver.
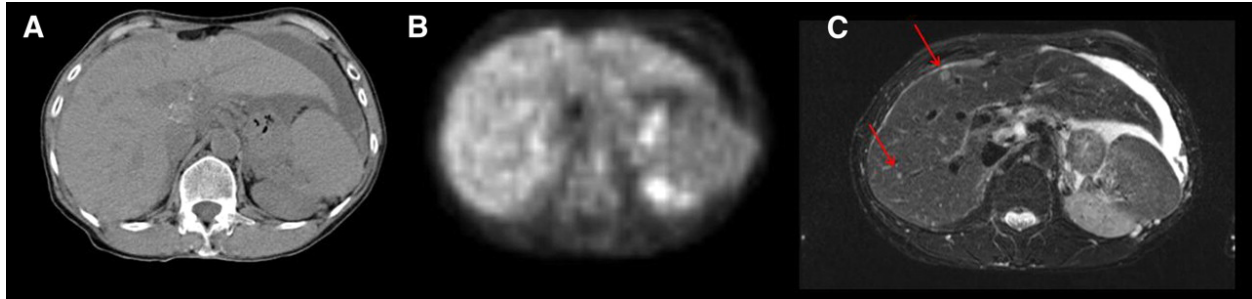Abdominal images of CT (A), 18F-FDG PET (B), and MRI (C) showing liver metastases detected by MRI but neither by CT, nor PET.[1]

Positron Emission Tomography (PET) is an emission-based functional imaging modality that utilizes a radiotracer probe that accumulates in a target tissue. The radiotracer probe produces positrons which then produce a pair of 511keV photons. PET has inherently poor resolution therefore any fine anatomic information is difficult to depict. The strength with PET imaging is that the radiotracer probes can be specially designed such that they target a specific metabolic pathway, or exploit certain functional characteristics of a tissue, localizing where these functions are active.

The most common radiotracer probe in use today is 18F-Flurodeoxyglucose or 18F-FDG. It exploits the high metabolic activity of malignant tumors that consume large amounts of glucose to power their activity. FDG is taken up by the tumors, however it is not metabolized and remains inside the tumor. Attaching Fluorine-18 to FDG converts it to a radiotracer probe, allowing localization of high FDG uptake. Tumor location can then be inferred from the PET image.

The block diagram for the PET image formation is shown in Figure 3. As part of the image reconstruction, an attenuation map (AC) should be provided. This attenuation map accounts for the attenuation that the photons experience as they travel through the body. When this information is provided, the PET image resolution is improved, and the radiotracer activity concentration estimate

is more accurate. Without the use of the attenuation map, the radiotracer activity concentration may be overestimated or underestimated, and this error may be spatially variable. This error is propagated to the quantitative modeling done. Figure 4 shows an attenuation-corrected PET image alongside a non-attenuation-corrected PET image.
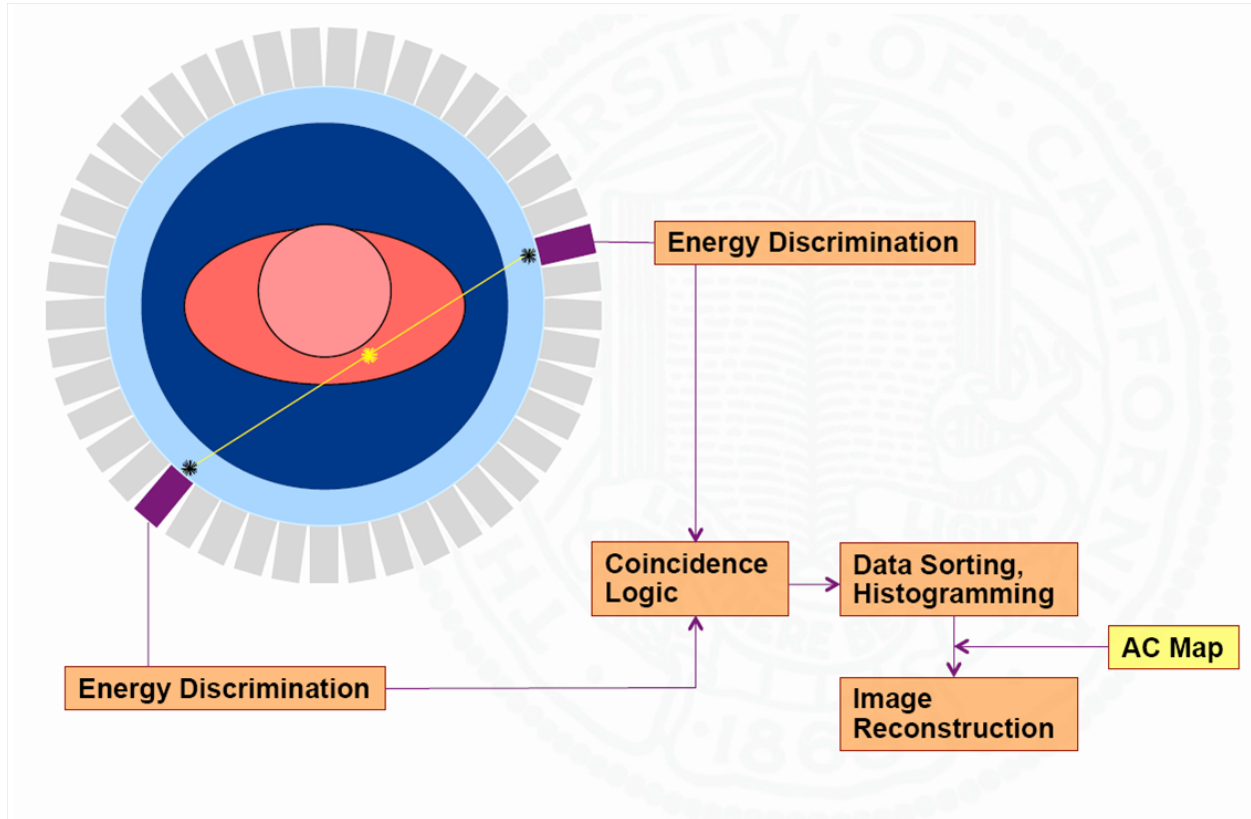
Figure 3: PET image formation block diagram.[2]
Emission from the PET radiotracer travels through the body and hits the detectors at opposite sides. The photons are detected and the data is pre-processed. The PET image is reconstructed with the acquired data.

An attenuation map is generated through the use of transmission imaging methods. On standalone PET scanners, a Ge-68 rod source is rotated around the patient. The data is reconstructed to produce the attenuation map. CT has replaced the Ge-68 rod source as the clinical gold standard for generating the attenuation map. With the ability of CT to generate the attenuation map, as well as function as its own imaging modality, PET/CT systems are now the standard and standalone PET scanners are rarely seen today.

The CT-derived attenuation map (CTAC) is generated by converting the CT HU values to the

Figure 4: Example of attenuation-corrected PET data
The top row shows attenuation-corrected PET data, and the bottom row displays
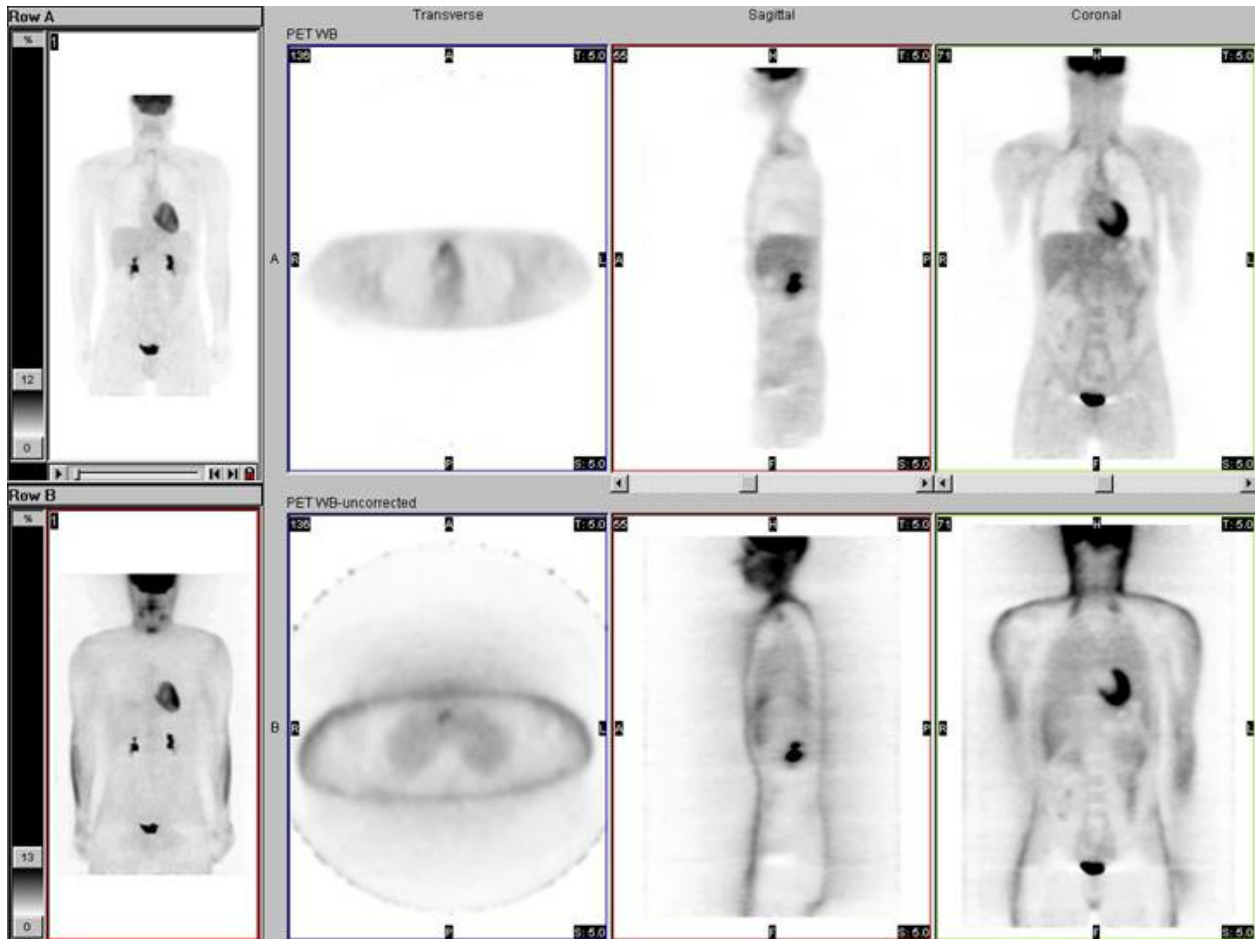non-attenuation-corrected PET data.[3] Darker intensity indicates more radiotracer uptake.
Qualitatively, it can be immediately seen that attenuation-corrected PET data provides better spatial
resolution, allowing better anatomic localization when viewing only the PET image.

PET 511keV linear attenuation coefficients (LAC). One method is using a piecewise linear model as shown in Figure 5. The CTAC is then filtered and downsampled to match the spatial resolution of the conventional PET rod source transmission image. A comparison of a PET transmission scan and a CTAC generated using a bilinear model is shown in Figure 6.

The combination of PET/CT and MRI is becoming increasingly common because of the soft-tissue contrast and multi-faceted imaging capabilities of MRI. Having a combined PET/MRI scanner avoids the difficulties associated with individual scans and then later combining them, such as image registration and physiologic state. In the patient's perspective, instead of having two individual PET
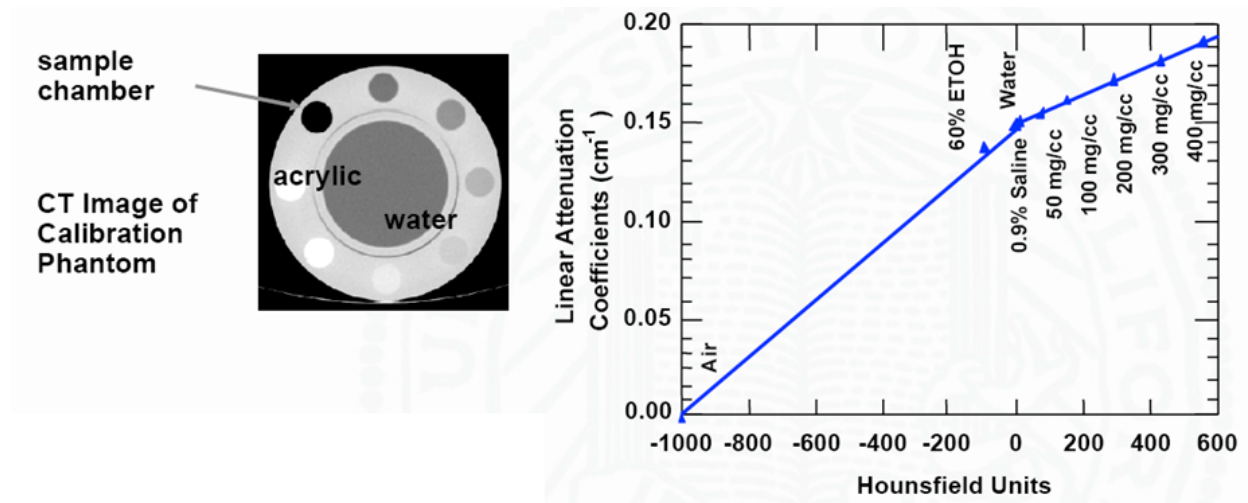
Figure 5: CT HU to 511keV Linear Attenuation Coefficients Model
A phantom containing different materials with known linear attenuation coefficients at 511keV (left) is scanned. A piecewise linear model is fitted (right) using the measured HU values from the CT image of the phantom.[4]

and MRI scans, only one scan is necessary with a combined PET/MRI scan. This would ensure that the patient's condition is consistent between the PET and MRI images.

The amount of dose a patient receives in a PET/CT scan highly dependent on the CT protocol. The dose contributed by PET is much lower compared to the dose contributed by the CT scan. [1] With whole-body imaging, the total dose to a patient may be considerable. Since MRI is a non-ionizing imaging modality, the use of PET/MR can greatly reduce the dose. This makes PET/MR more viable for high-risk populations for radioactive dose such as children or patients requiring many imaging studies.

One of the major challenges of PET/MR is the generation of the attenuation map. The attenuation map provides the information that allows the image reconstruction algorithm to correct for the attenuation that photons experience as they travel from source to detector. With PET/CT systems, the information is directly sampled, which cannot be done with MRI. The attenuation map must then be derived from the MR images.

To assess the requirements of an MR attenuation coefficient map, Ouyang et al explored the effect of tissue misclassification on the PET activity concentration.[6] Different tissue classes were derived and segmented from the CT images acquired with a PET/CT scanner. The following classes
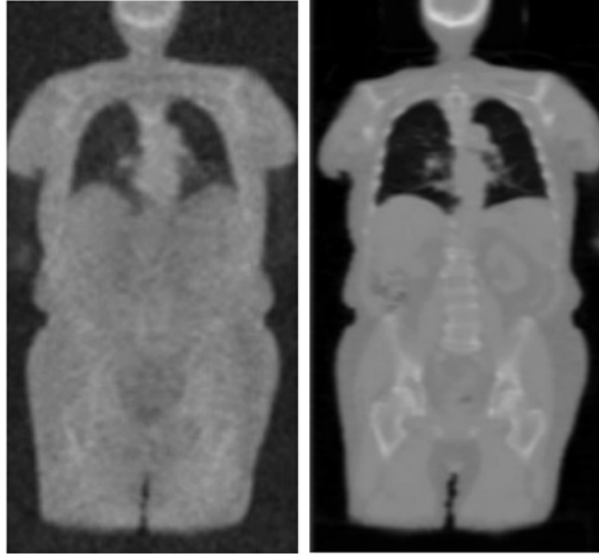
Figure 6: PET Attenuation Maps

A PET transmission scan (left), and a CTAC (right) generated using a bilinear model.[5] The CTAC has greater signal-to-noise and better spatial resolution. However, the CTAC can introduce biases in the attenuation-corrected PET image if an inappropriate model was used to generate the CTAC.

Segmentation Map	Tissue Classes
3-class	Air, Lung, Other Tissues
4-class	Air, Lung, Fat, Non-fat Soft Tissues
5-class	Air, Lung, Fat, Water, Bone

Table 1: CT-derived Segmentation Map Components

were defined: air, lungs, fat, non-fat soft tissues, and bones. From these tissue classes, 3-class, 4-class, and 5-class segmentation maps were generated. The components of each class are listed in Table 1, and their results are shown in Figure 7

From a 3-class map to a 4-class map, considering fat in the attenuation coefficient map, the root-mean-square error (RMSE) of the PET activity in voxels around fatty regions was reduced by 12.8%, and voxels around bony regions was reduced by 5.7%. With a 5-class map, considering bone, the RMSE of voxels around bony regions was further reduced by 5%. Their results suggest that error occurs when voxels are surrounded by misclassified tissues. The error is significantly reduced for voxels surrounding tissues that have their own class.

There are multiple ways proposed to generate the MR-based attenuation map (MRAC). These include template-based or atlas-based, patient-derived from specific MR pulse sequences, or a

MEAN, STANDARD DEVIATION, AND RMSE OF VOXEL-WISE BIAS FOR EACH TISSUE CLASS FOR THE CT-BASED STUDY [MEAN±STANDARD DEVIATION (RMSE)]

Root-mean-square error in (parentheses)

method	lungs	fat	non-fat soft tissues	bones
3C	5.8 ± 14.6% (15.7%)	14.2 ± 9.3% (16.9%)	-0.8 ± 8.0% (8.0%)	-15.4 ± 10.5% (18.6%)
(Fat added) 4C	4.4 ± 14.4% (15.1%)	2.5 ± 3.2% (4.1%)	4.0 ± 5.3% (6.6%)	-9.0 ± 9.2% (12.9%)
(Bone added) 5C	4.5 ± 14.2% (14.9%)	1.2 ± 2.7% (3.0%)	0.2 ± 3.0% (3.0%)	-0.1 ± 7.9% (7.9%)

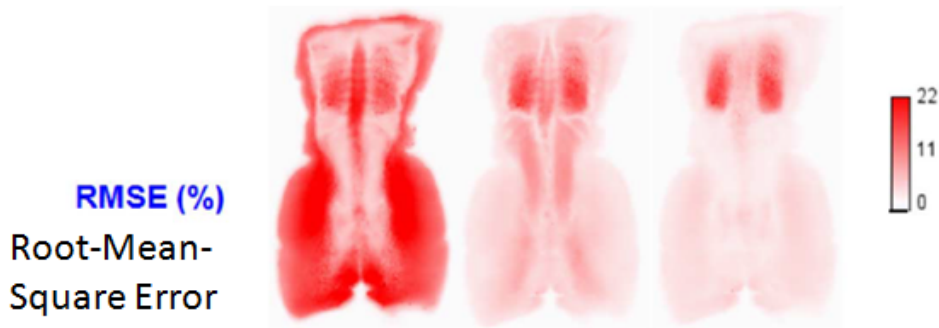12.8%   5.7%   5%   10.7%

RMSE (%) Root-Mean-Square Error

Figure 7: Errors produced by not considering certain tissue classes.
The table shows the root-mean-square error for different numbers of classes. The errors are mapped out in the images of the body.[6]

combination of these methods.[7]

Template-based or atlas-based methods generate a template or an atlas from a patient population. This template or atlas is registered to the MR image of the patient to derive an AC map. This allows for an attenuation map with continuous values. The major caveat of this method is that it does not fully account for patient-specific variability in tissue structure and density. The method also relies heavily on the quality of the template or atlas, and the registration to the patient's image.

Special MRI pulse sequences such as Dixon, Ultrashort Echo Time (UTE), or Zero Echo Time (ZTE) are currently being used for MRAC. However, the caveat of using these methods is that current methods do not account for all the possible tissue classes. The Dixon-based sequences only classify air, fat, and water, and do not classify bone. UTE/ZTE sequences can only classify air, bone, and soft tissue, and do not separate soft tissue into fat and water.

7

These methods can be combined, but this would be susceptible to registration errors. Obtaining the complete attenuation map from only a single MR image would eliminate registration biases, be very time-efficient, and obtain patient-specific information as well.

The current ZTE-based MRAC generation method only uses the magnitude image for MRAC generation,[8] and classifies air, bone, and soft tissue, but does not separate soft tissue into fat and water. It is commonly known that phase accumulation is proportional to the echo time (TE), and with zero echo time, by conventional wisdom there is no phase accumulation. However, phase accumulation is still present for UTE images,[9] and ZTE images. This is the result of phase accumulation occuring during the readout.
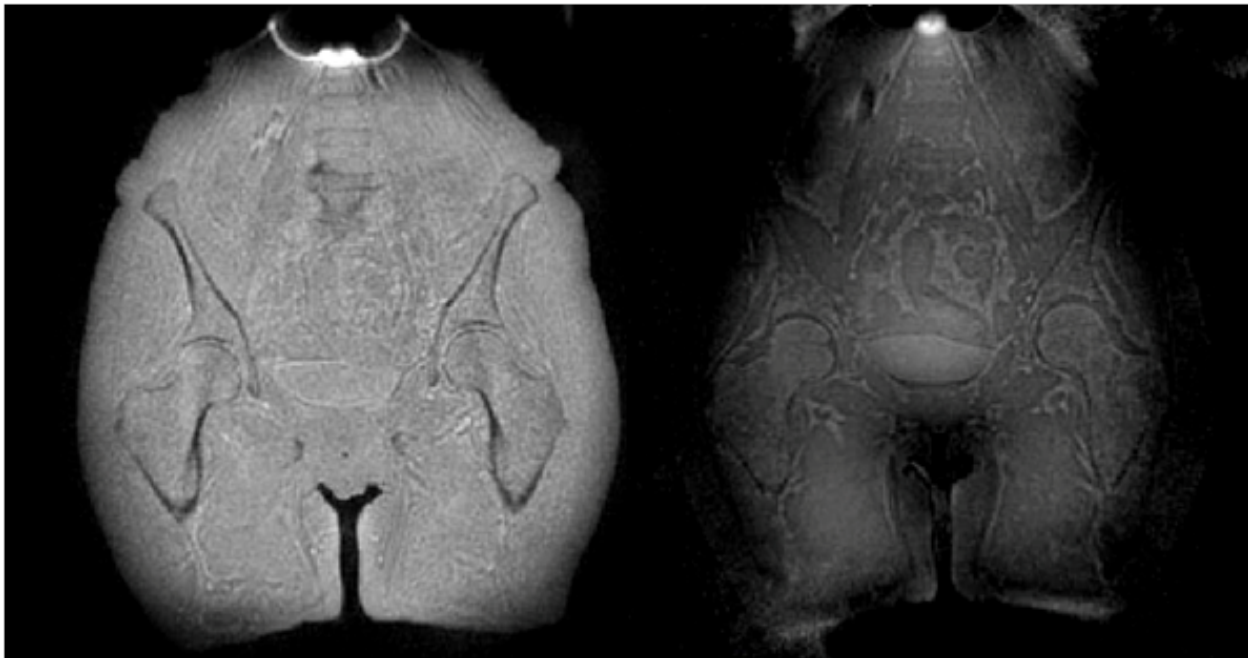
Figure 8: ZTE magnitude and phase images.
It can be seen from the phase image (right) that there is phase contrast present that is not visible in the magnitude image (left). This phase contrast would allow soft tissue to be separated into fat and water components.

Figure 8 shows the ZTE magnitude and phase images in the pelvis. From the phase image, it can be seen that there is phase contrast between fat and water. With this additional phase information, we believe bone, air, fat, and water may be segmented and classified for the attenuation map from only a single scan, avoiding the registration errors encountered when two separate scans are required

and resulting in a very time-efficient method, if done automatically.

For this thesis, generating a pseudo-CT image of the pelvis is the main focus as it has a significant amount of bone, air, fat, and water. These tissues would contribute significantly to the PET reconstruction and therefore, all the components must be considered.

The goal is to segment and classify 5 tissue classes from a single ZTE scan: bone, air, and soft tissue can be segmented from the magnitude image. Soft tissue is further separated into fat and water components using the phase image.

2 Methods

2.1 Image Acquisition

Pelvis images of a single patient was obtained from the PET/MR Technology Development (ISR01) study. The study was approved by the institutional review board, and all patients signed an informed consent form. MR images of the pelvis were acquired using a 3T General Electric Signa TOF-PET/MR scanner (GE Medical Systems, Waukesha, WI, USA) using a 26-channel flexible body coil at the UCSF Imaging Center at China Basin Landing.

2.2 MRI ZTE Pulse Sequence

The ZTE pulse sequence is a pulse sequence where the echo time (TE) is zero. This is achieved by applying a hard RF pulse while the gradients are active, and doing radial center-out k-space sampling.

As the scanner cannot instantaneously switch between excitation and readout, there are samples around the center of k-space which are not acquired. This time period is called the dead time (ΔT). The unsampled k-space region is acquired by running the sequence again, but with smaller gradient amplitudes, the so-called water- and fat-suppressed proton projection MRI (WASPI) method.[10] However, there would still be an unsampled region at the center of k-space. This much smaller
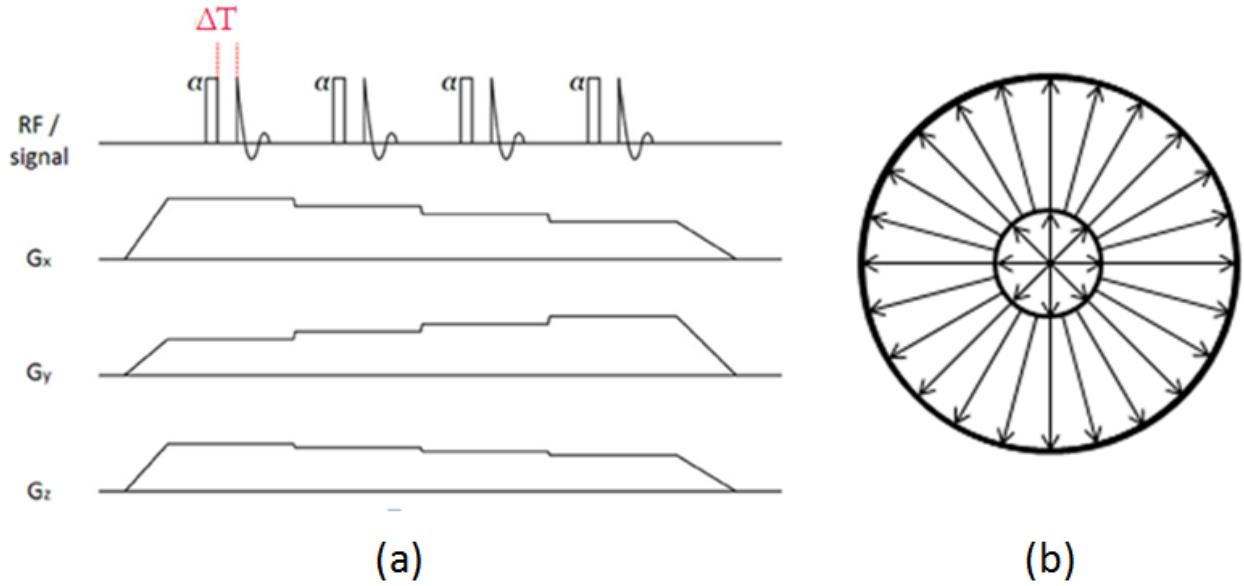
Figure 9: ZTE pulse sequence timing diagram and k-space sampling pattern.
The ZTE timing diagram[8] (a) shows the pulse sequence waveforms. The gradients are already turned on when RF excitation is applied. There is a dead time ΔT where the scanner is not able to acquire data. Missing k-space data is acquired by repeating the sequence with lower gradient amplitudes[10] giving the k-space sampling pattern shown in (b).

unsampled region is filled in through interpolation and gridding reconstruction. The timing diagram and k-space sampling pattern of the ZTE pulse sequence is shown in Figure 9. ZTE is a 3D imaging method. The scan parameters used are listed under Table 2.

Dead time (ΔT)	8μs
Resolution	2mm isotropic
Field-of-View (FoV)	34cm x 34cm
Bandwidth	$\pm$62.5kHz
Flip angle	$1°$
Weighting	Proton-density

Table 2: ZTE scan parameters used.

2.3   MRI Image Reconstruction

Acquisition of the images is done using multi-channel coils. The individual coil images need to be combined to produce the final image.

2.3.1 Magnitude Image

The magnitude image is reconstructed using the sum-of-squares method given by the equation:

$$M = \sqrt{\sum_{j=1}^{N} M_j^2} \tag{1}$$

where M is the final combined magnitude image, and M_j is the magnitude image of the channel. This method accounts for the differences in coverage and SNR of each coil channel. This method provides high SNR without acquiring the individual coil sensitivity maps. However, the phase information is discarded and must be reconstructed separately.

2.3.2 Phase Image

The phase image is reconstructed using the following equation:[11]

$$\phi = \angle(\sum_{j=1}^{N} \frac{M_j}{M} e^{i\phi_j^{corrected}}) \tag{2}$$

where M_j is the magnitude image of the channel, M is the combined magnitude image, and $\phi_j^{corrected}$ is the unwrapped and high-pass filtered phase image of the channel.

The phase of a voxel is constrained to values within $-\pi$ and $+\pi$. When the actual phase goes beyond these values, the phase is shifted by 2π, causing otherwise smooth curves to be discontinuous causing "wrapping", as shown in Figure 10. Unwrapping the phase image obtains the original phase and eliminates the discontinuity. High-pass filtering removes the constant phase offset that may be present in each channel. This method of coil combination accounts for the differences in SNR and only uses the phase information from voxels with enough SNR.

Phase unwrapping and high-pass filtering can be done simultaneously using homodyne filtering.[12][13] The corrected coil channel phase image is given by the equation:

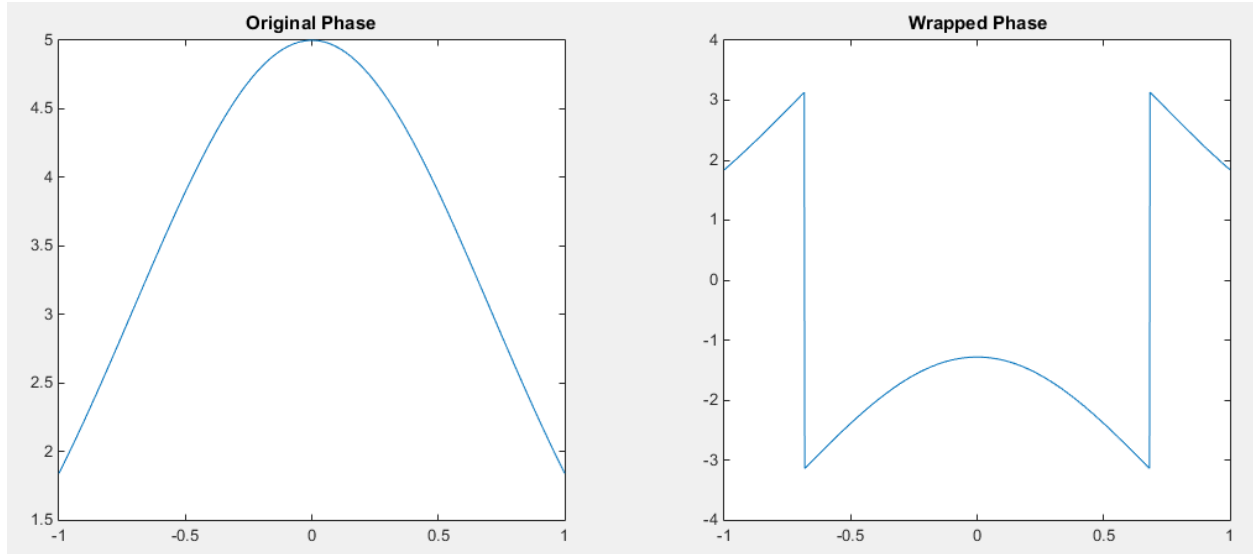$$\phi_j^{corrected} = \angle(\frac{C_j}{\text{LPF}[C_j]}) \tag{3}$$

Figure 10: Phase wrapping
An example of the original phase (left) is becoming wrapped (right) when the phase is acquired.

where C_j is the complex image of the channel, and LPF is the low-pass filtering operation.

2.4 Image Pre-processing

To improve image quality, the images were low-pass filtered to reduce noise. A 3x3x3 3D Gaussian filter with a variance of 3 was used.

2.4.1 Magnitude Image

N4 bias correction[14] is applied to remove the bias field to make the signal intensities more homogenous. Histogram-based intensity correction[8] was used to further correct for the intensity and to normalize the maximum image intensity to soft tissue.

2.4.2 Phase Image

Background field removal was done by treating the phase image as a magnitude image and applying N4 bias correction. By using N4 bias correction instead of filtering methods, the background field can be eliminated without removing the low-frequency phase information.

2.5   Segmentation and Classification

Semi-automated segmentation and classification methods have been developed to identify the four tissue classes (bone, air, fat, water) from the magnitude and phase images. The different tissue types are segmented based on signal intensity and spatial location.

2.5.1   Air Segmentation

Between outside air and the tissue, there is a distinct shift in image intensity. Outside air was segmented using an intensity-limited region-growing algorithm on the intensity corrected magnitude image. A seed was automatically placed on the edge of the image and the intensity limit for the region-growing was determined empirically.

An issue we faced is that bowel air has overlapping signal intensities with bone. However, for the pelvis, bone and air are anatomically in separate areas. Bowel regions were defined manually by selecting the region of interest axially, slice-by-slice. Thresholding was done inside the defined bowel regions. The threshold value that qualitatively gives the optimal air and soft tissue segmentation is determined empirically.

2.5.2   Bone Segmentation

The process of bone segmentation is outlined in Figure 11. High-pass filtering using a Gaussian filter was first done to enhance the edges. Logarithmic intensity rescaling enhances the bone while maintaining soft tissue contrast and produces a CT-like image.[8] Top-Hat morphological filtering with a 2mm radius sphere picks out the edges and removes the background. Global thresholding was applied on the top-hat filtered image. The threshold value was empirically determined that gives the most bone depiction with the least noise possible. Morphological area opening was used to eliminate small objects. The object size for the area opening was empirically determined. The segmentation map was then manually corrected.
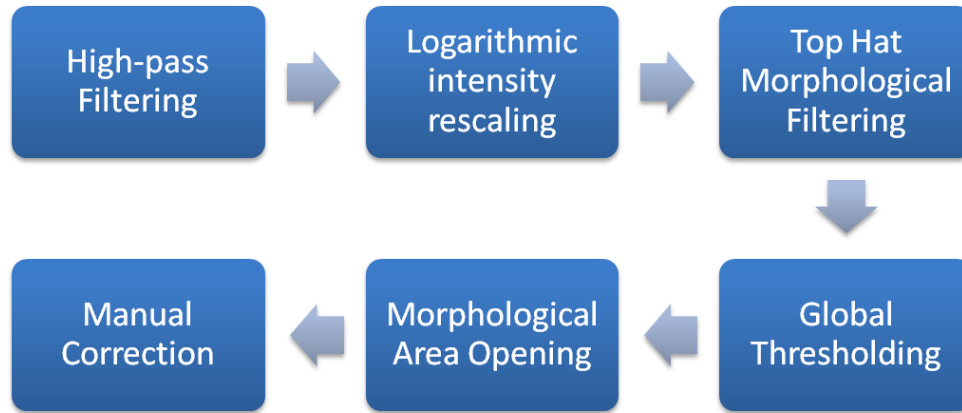
Figure 11: Bone segmentation process.

2.5.3 Soft Tissue Segmentation

After bone and air segmentation is achieved, soft tissue is simply the remaining voxels where bone and air are not present. Mathematically:

$$\text{Soft Tissue} = (NOT(\text{Bone}))AND(NOT(\text{ Air})) \tag{4}$$

2.5.4 Fat-Water Segmentation

Fat and water are classified from the phase image using the soft tissue segmentation mask generated from the magnitude image. Fuzzy c-means clustering is used to do soft segmentation. This is to achieve a continuous value fat-water map similar to the Dixon-type fat-water map, instead of assigning fixed values to fat and water. Providing a continuous value map is more accurate than applying fixed values to fat and water.[15] Figure 12 outlines the fat-water segmentation.

2.6 Pseudo-CT Generation and PET Reconstruction

The pseudo-CT image is generated by combining the segmentation maps of each tissue type. Bone, inside air, and outside air voxels are assigned fixed HU values. Fat and water voxels are assigned an HU value based on the following equation:[15]
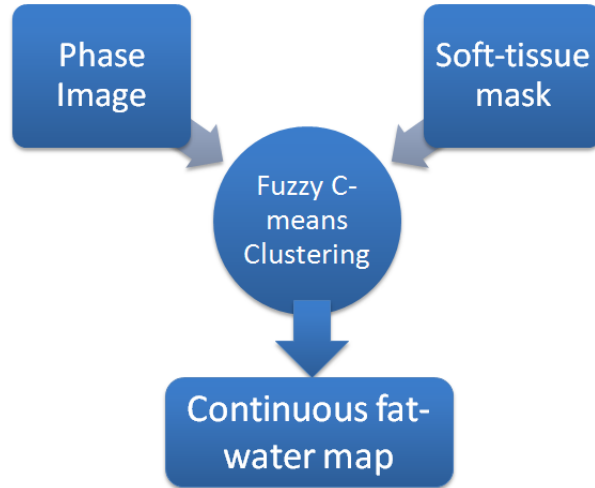
Figure 12: Fat-water segmentation diagram.

$$\text{FatWaterHU} = \text{FatHU} * \text{Fat Fraction} + \text{WaterHU} * \text{Water Fraction} \tag{5}$$

2.7 MRAC Evaluation

The generated ZTE pseudo-CT is evaluated by qualitatively comparing it to the patient's CT images, and the MRI Dixon-derived fat-water map. The Dixon fat-water map is the currently used standard for MRAC in the body (not brain) on PET/MR scanners. Figure 13 and Figure 14 show the CT image and the Dixon MRAC, respectively.

3 Results

Pelvis images were acquired using the ZTE pulse sequence with the stated scan parameters and the reconstructed images are shown in Figure 15. Coil combination took several minutes at the specified resolution and number of coils. Because of the bias fields that are present in the images, there would be large variations in signal intensity for the same tissue type, as well as overlapping signal intensities between different tissue types. The relevant tissue classifications cannot be easily segmented.
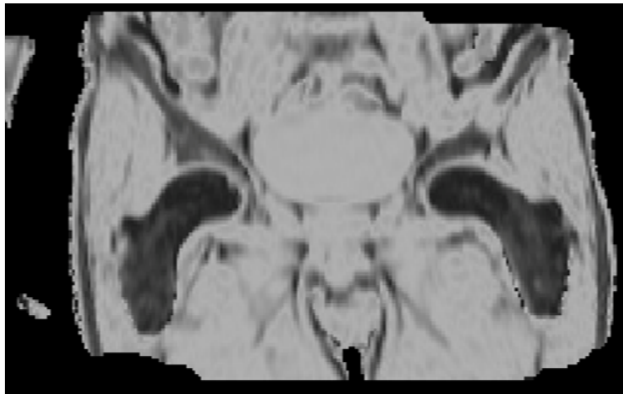
Figure 13: CT image of the pelvis.

Figure 14: Dixon Continuous Fat-Water MRAC.

To prepare for image segmentation, the pre-processing steps were applied on the acquired images. 3D slicer [16][17] was used to apply N4 bias correction, and histogram-based intensity correction was applied using in-house developed software. The pre-processing only takes a couple of minutes to complete. The pre-processed images are shown in Figure 16. The bias fields of the magnitude and phase images have been eliminated and the images can then be segmented.

The mask selecting the bowel regions is shown in Figure 17. Within this mask, bowel air is segmented and the result is shown in Figure 18. Coronal slices of each step of the bone segmentation processing (process shown in Figure 11) is shown in Figure 19. Combining the results of the bone and air segmentation, the soft tissue can then be segmented and shown in Figure 20. Using the soft tissue mask and the ZTE phase image, the continuous fat-water map was then clustered and the
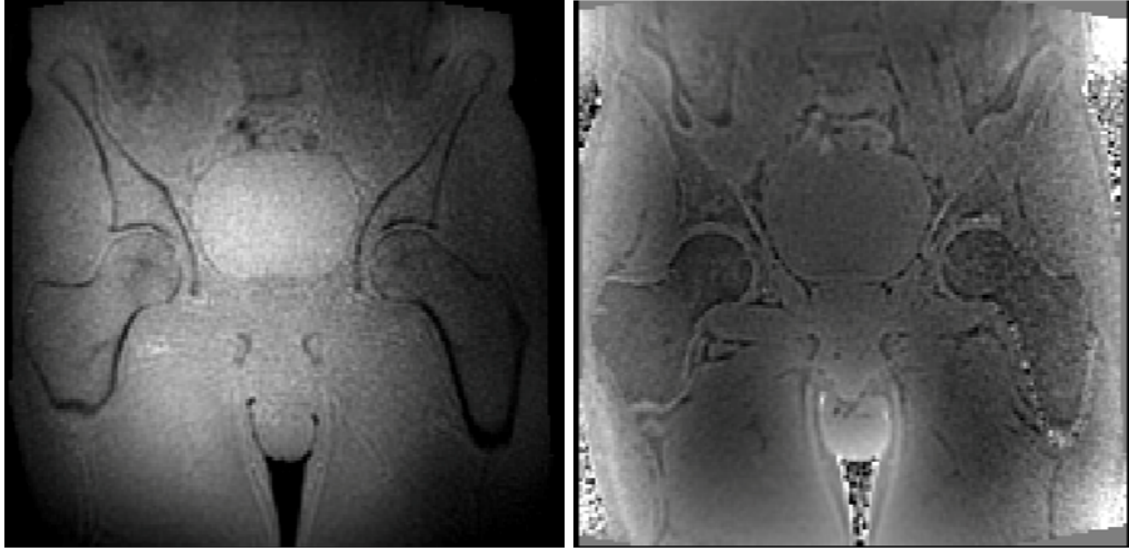
Figure 15: Acquired ZTE magnitude and phase images of the pelvis.
The bias field of the magnitude image (left) is indicated by the brighter intensity in the middle of
the image compared to the edge of the image. The phase background field in the phase image
(right) is indicated by the brighter intensity towards the edge of the body.

result in shown in Figure 21. Majority of the time spent in producing the segmentation maps are in the manual selection of the bowel regions, taking approximately 30 minutes, and the manual correction of the bone segmentation, taking several hours. From these segmentation maps, the final pseudo-CT is then generated and is shown in Figure 22.

4 Discussion

The ZTE pseudo-CT is shown side-by-side with the CT image at approximately the same slice location with a coronal view in Figure 23, and with a sagittal view in Figure 24.

The bone segmentation was able to easily account for the thicker cortical bone, for example around the shaft of the femur. However, the segmentation was having trouble in identifying the cortical bone at the lumbar, and the bone inside the femur. This is due to the difficulty in depicting thin cortical bone in the original ZTE magnitude image that has 2mm isotropic resolution. Figure 25 shows areas where cortical bone was difficult to distinguish from the surrounding soft tissue.

Partial volume and chemical shift effects are identified as possible causes of poor thin cortical
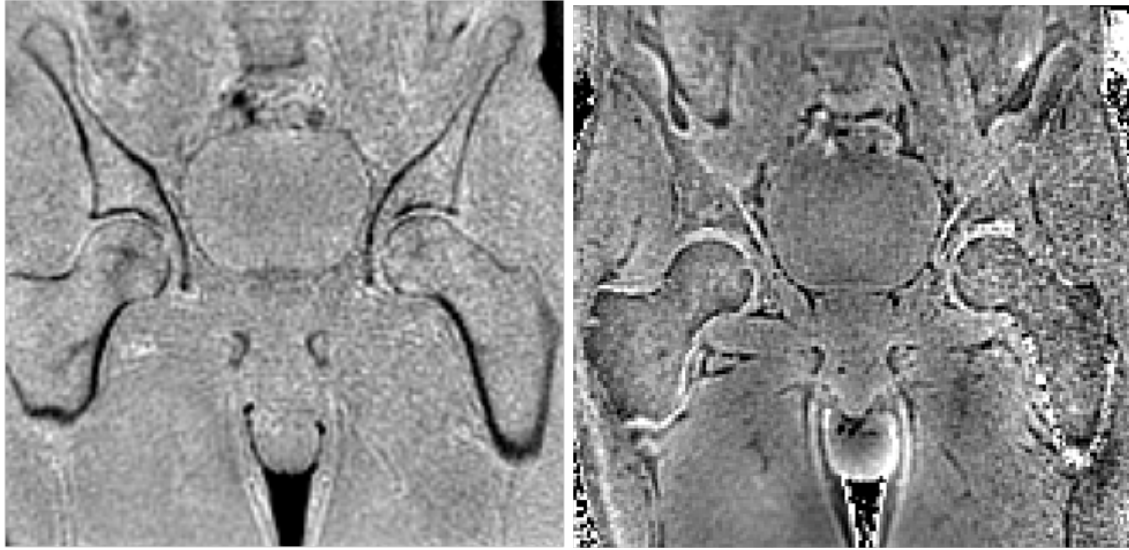
Figure 16: Pre-processed ZTE magnitude and phase images of the pelvis.
As compared to the original acquired images, the bias field of the magnitude image (left) and background field of the phase image (right) have been eliminated.

bone depiction. Because of the imaging resolution used, the cortical bone may be too thin to be able to be separated from the neighboring soft tissue. Chemical shift in the ZTE scan would also cause blurring of the fatty bone marrow signal, making it overlap with the cortical bone. It is currently unknown how much of this thin cortical bone would affect the PET image. A possible solution is using an atlas-guided approach where the atlas would identify the probable location of bone, and then soft thresholding would be done. This could allow for the identification of cortical bone, and account for the overlapping signal due to the partial volume and chemical shift effects.

The air in the large intestine was easily accounted for, while the air in the small intestine was more difficult to depict. The probable reasons for this are motion and partial voluming. The large intestine was further away from the diaphragm than the small intestine. This causes motion and partial volume effects, making the signal from air and soft tissue mix together. The ZTE acquisition lasts a few minutes while the CT is on the order of seconds, accurately capturing the anatomy at that specific moment of time. The following could be a possible solution: instead of using simple thresholding and assigning a fixed HU value for soft tissue and bowel air, fuzzy c-means clustering and a continuous mapping of soft tissue and bowel air HU values could be done inside the bowel
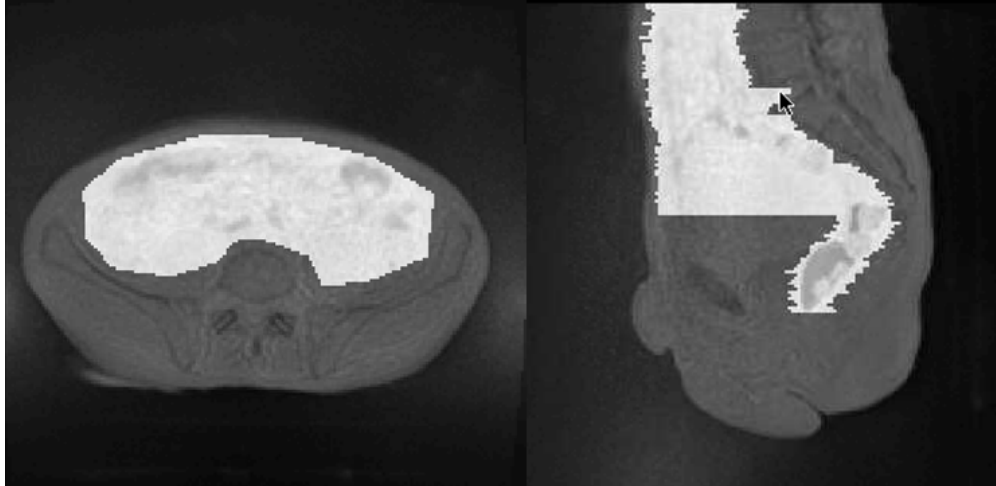
Figure 17: Defined bowel regions.
Axial (left) and sagittal (right) views of the binary mask selecting the bowel regions superimposed on the magnitude image.

Figure 18: Air segmentation results.
Axial (left) and sagittal (right) slices of the air segmentation result.

regions, similar to a continuous fat-water separation. Voxels that have high probability of being soft tissue would then be separated into fat and water components.

The Dixon fat-water map is the currently used standard attenuation map for PET/MR body imaging. Figure 26 shows the comparison of the ZTE pseudo-CT to the Dixon fat-water pseudo-CT. A major advantage of the ZTE pseudo-CT over the Dixon fat-water is that the ZTE pseudo-CT accounts for bone, which contributes a significant amount of attenuation. Small pockets of fat were well segmented while large homogenous regions such as muscle in the leg, the bladder, and inside the bone were not segmented well by our current methods.
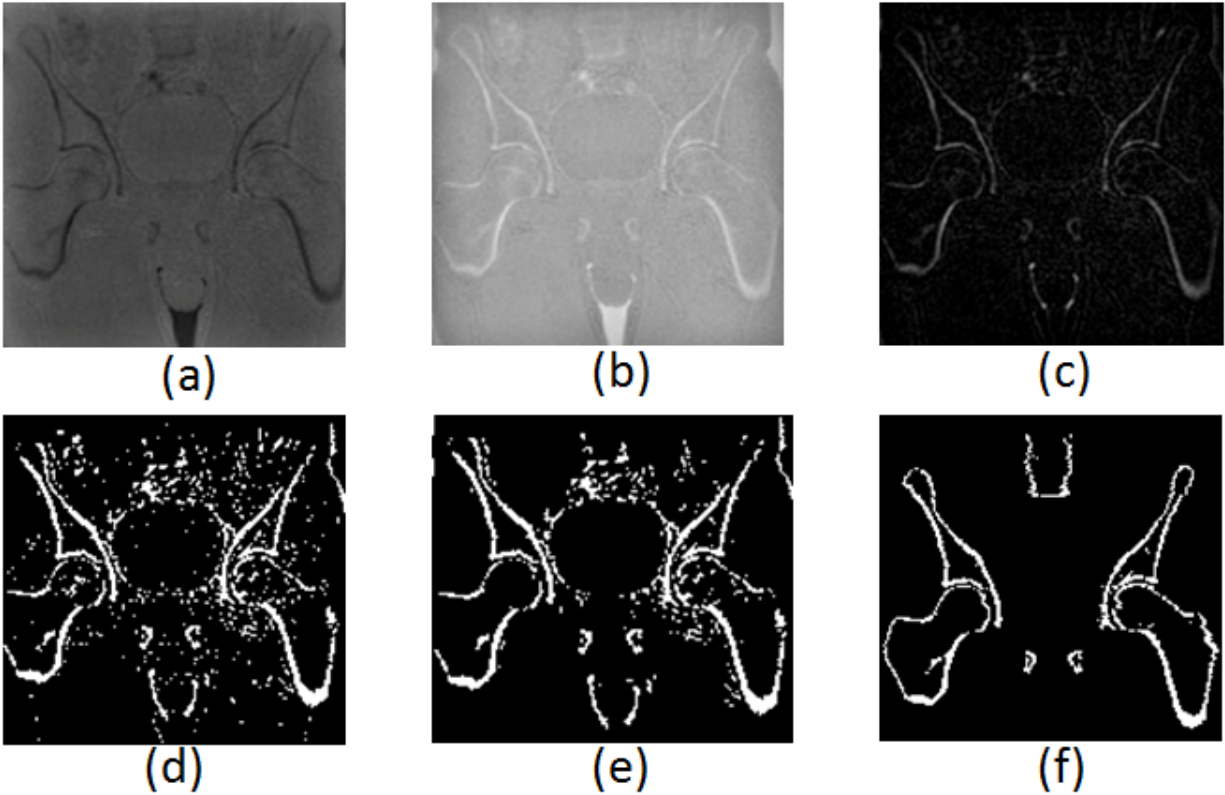
19

Figure 19: Bone segmentation results based on the process outlined in Figure 11. Step-by-step results of the bone segmentation. High-pass filtering (a), Logarithmic intensity rescaling (b), Top-hat morphological filtering (c), global thresholding (d), morphological area opening (e), and manual correction (f).

The k-space sampling trajectory of the ZTE pulse sequence makes the ZTE phase image inherently high-pass filtered. K-space is sampled in a radial center-out trajectory, and the phase accumulates during the readout. Larger features, which have more points near the center of k-space, would then have less phase accumulated as compared to smaller features, which have more points at the outer part of k-space. Edges are enhanced and large homogenous regions have low phase contrast. Possible ways to improve the phase contrast would be explored in order to better generate the fat-water map. One suggestion is to repeat the ZTE acquition, but with different bandwidth. This change in bandwidth would give different phase accumulation, and an algorithm similar to a Dixon-type fat-water decomposition may be used.

Given the trade-offs in resolution, bandwidth, scan time, signal-to-noise (SNR), and other factors, it is difficult to identify any single answer to each of the problems stated above. More

Figure 20: Soft tissue segmentation results.

research needs to be done to identify and explore the possible solutions or alternative methods to properly generate an accurate pseudo-CT.

5 Conclusion

An MR-derived attenuation correction (MRAC) pseudo-CT map has successfully been derived from a single ZTE image: bone, air, and continuous fat-water classifications are present. The ZTE MRAC pseudo-CT map is qualitatively similar to the CT image and Dixon fat-water pseudo-CT map, however, the results are still preliminary and there is much room for improvement. In order to have a better understanding of the results and the fundamental requirements for MRAC accuracy and precision, a PET image needs to be reconstructed using the ZTE-derived MRAC, and quantitatively compared against PET images produced using CT-derived attenuation correction (CTAC) and Dixon MRAC.
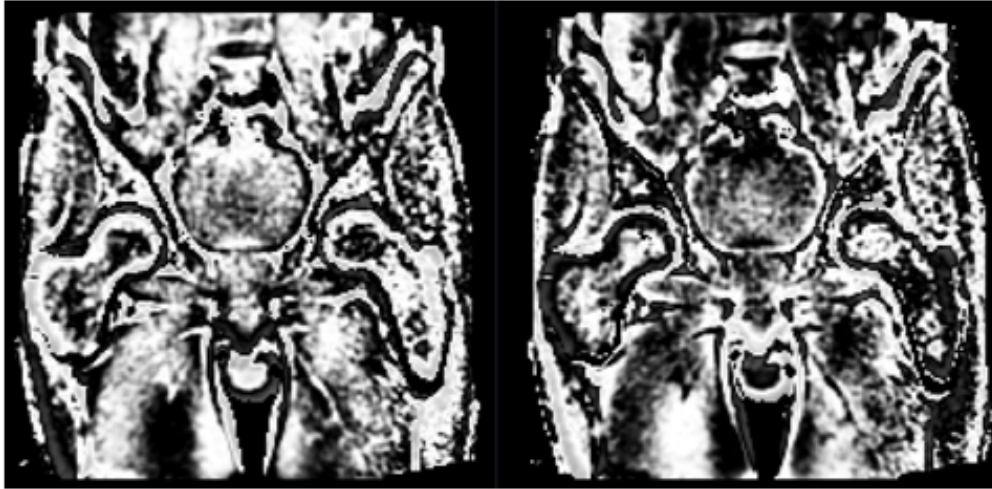
Figure 21: Continuous value fat-water soft segmentation results obtained by the process outlined in Figure 12.
The water (left) and fat (right) maps have values between 0 and 1 indicating the fraction of fat and water that a voxel has.
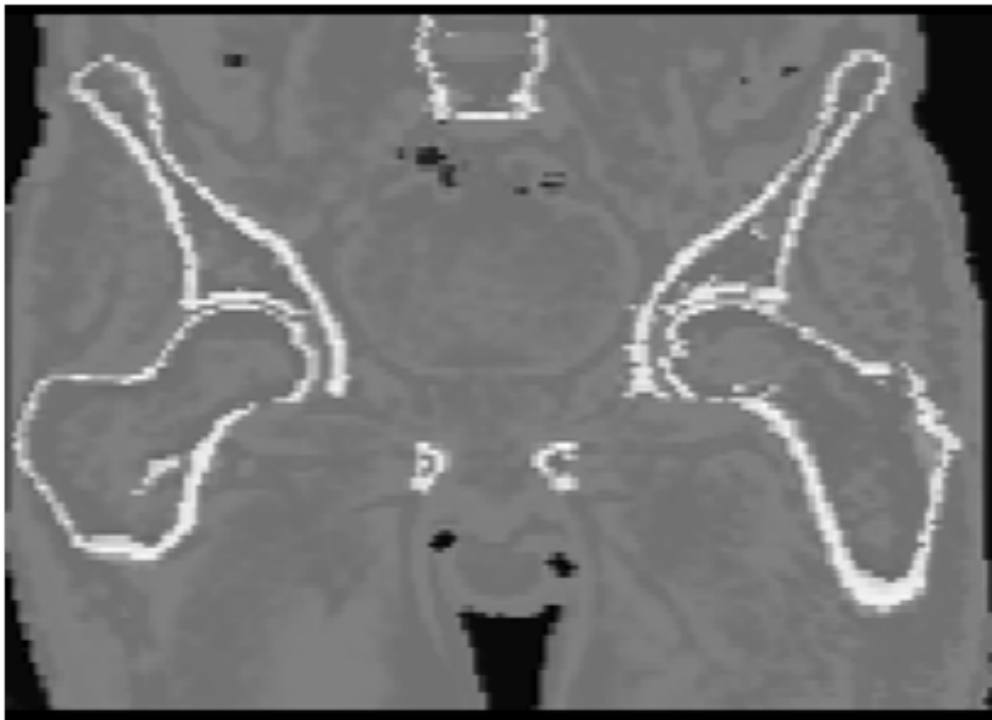

Figure 22: ZTE Pseudo-CT.
Generated ZTE pseudo-CT from the bone, air, fat, and water segmentation maps.

Figure 23: ZTE Pseudo-CT and CT comparison highlighting bone.
The ZTE Pseudo-CT (left) is compared with CT (right). The blue arrow indicates the portion of cortical bone that the ZTE pseudo-CT is able to account for. The red arrow points to the lumbar where the cortical bone was not accounted for in the ZTE Pseudo-CT. The orange arrow indicates the inside of the bone where there is significant attenuation, but was not accounted for in the ZTE pseudo-CT.
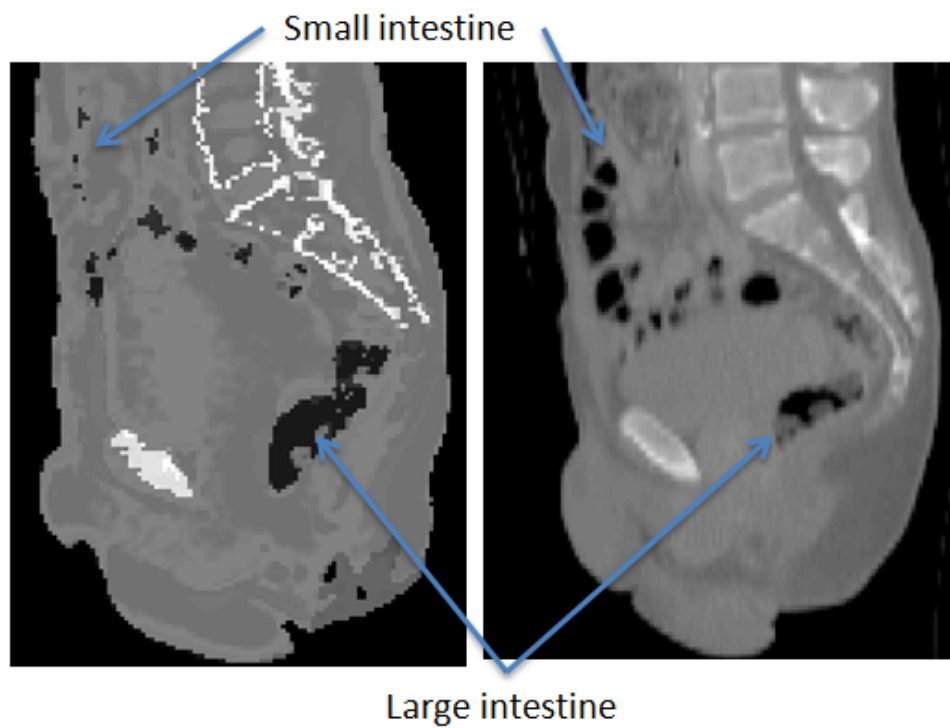
Figure 24: ZTE Pseudo-CT and CT comparison highlighting air.
ZTE Pseudo-CT (left) compared with CT (right). The blue arrows are pointing at bowel air in the small intestine, and large intestine. The bowel air segmentation in the small intestine did not perform as well as in the large intestine, although some differences may be due to the time delay between the PET/MRI and CT scans.

Figure 25: ZTE bone depiction.
Regions of thin cortical bone are difficult to distinguish from the surrounding soft tissue due to the resolution achievable with ZTE MRI. Attenuation inside the bone is difficult to account for in the magnitude image due to the fact that these voxels contain a large fatty, soft tissue fraction (bone marrow), as well as trabecular bone.
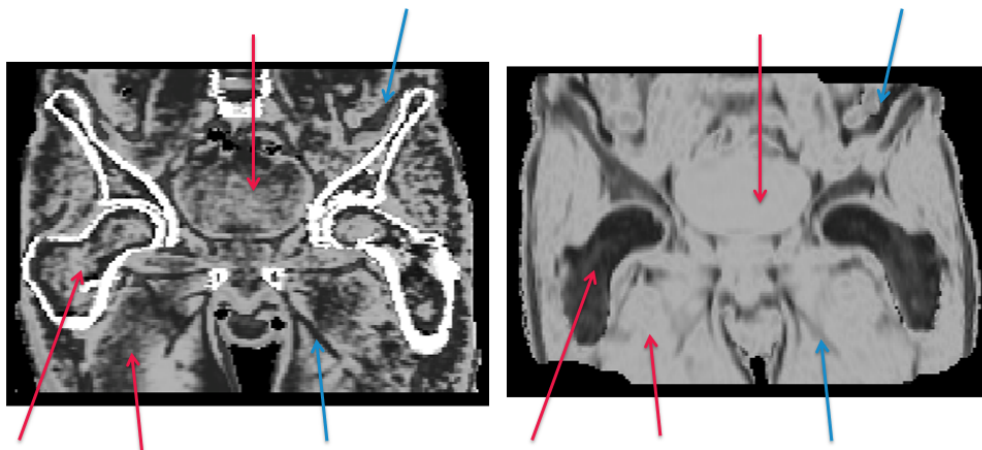

Figure 26: ZTE Pseudo-CT and Dixon Pseudo-CT comparison of fat-water map
ZTE Pseudo-CT (left) compared with Dixon pseudo-CT (right). The blue arrows are pointing at features which were well accounted for, while the red arrows are pointing at regions which were not segmented well by the ZTE Pseudo-CT.

References

1. Pichler, B. J., Kolb, A., Thomas Nägele & Schlemmer, H.-P. PET/MRI: Paving the Way for the Next Generation of Clinical Multimodality Imaging Applications. *Journal of Nuclear Medicine* **51,** 333–336. ISSN: 0161-5505, 2159-662X (Mar. 1, 2010).

2. Seo, Y. *BI 202 Lecture 6: PET Instrumentation, Coincidence Imaging Lecture Notes* 2014.

3. *PET/CT* <https://www.med-ed.virginia.edu/courses/rad/PETCT/Attenuation.html> (2015).

4. Seo, Y. *BI 202 Lecture 9: SPECT/CT and PET/CT (and PET/MR and SPECT/MR)* 2014.

5. Ay, M. R., Shirmohammad, M., Sarkar, S., Rahmim, A. & Zaidi, H. Comparative Assessment of Energy-Mapping Approaches in CT-Based Attenuation Correction for PET. *Molecular Imaging and Biology* **13,** 187–198. ISSN: 1536-1632, 1860-2002 (Apr. 13, 2010).

6. Ouyang, J. *et al.* Bias Atlases for Segmentation-Based PET Attenuation Correction Using PET-CT and MR. *IEEE Transactions on Nuclear Science* **60,** 3373–3382. ISSN: 0018-9499 (Oct. 2013).

7. Wagenknecht, G., Kaiser, H.-J., Mottaghy, F. M. & Herzog, H. MRI for attenuation correction in PET: methods and challenges. *Magnetic Resonance Materials in Physics, Biology and Medicine* **26,** 99–113. ISSN: 0968-5243, 1352-8661 (Nov. 21, 2012).

8. Wiesinger, F. *et al.* Zero TEMR bone imaging in the head. *Magnetic Resonance in Medicine,* n/a–n/a. ISSN: 1522-2594 (Jan. 1, 2015).

9. Carl, M. & Chiang, J.-T. A. Investigations of the origin of phase differences seen with ultrashort TE imaging of short T2 meniscal tissue. *Magnetic Resonance in Medicine* **67,** 991–1003. ISSN: 1522-2594 (Apr. 1, 2012).

10. Wu, Y. *et al.* Water- and fat-suppressed proton projection MRI (WASPI) of rat femur bone. *Magnetic Resonance in Medicine* **57,** 554–567. ISSN: 1522-2594 (Mar. 1, 2007).

11. Rauscher, A., Haacke, E. M., Neelavalli, J. & Reichenbach, J. R. in *Susceptibility Weighted Imaging in MRI* (eds Haacke, E. r. & Reichenbach, J. R.) 47–71 (John Wiley & Sons, Inc., 2011). ISBN: 978-0-470-90520-3. <http://onlinelibrary.wiley.com/doi/10.1002/9780470905203.ch4/summary> (visited on 06/03/2015).

12. Rauscher, A. *et al.* Improved elimination of phase effects from background field inhomogeneities for susceptibility weighted imaging at high magnetic field strengths. *Magnetic Resonance Imaging* **26,** 1145–1151. ISSN: 0730-725X (Oct. 2008).

13. Noll, D., Nishimura, D. & Macovski, A. Homodyne detection in magnetic resonance imaging. *IEEE Transactions on Medical Imaging* **10,** 154–163. ISSN: 0278-0062 (June 1991).

14. Tustison, N. *et al.* N4ITK: Improved N3 Bias Correction. *IEEE Transactions on Medical Imaging* **29,** 1310–1320. ISSN: 0278-0062 (June 2010).

15. Wollenweber, S. *et al.* Comparison of 4-Class and Continuous Fat/Water Methods for Whole-Body, MR-Based PET Attenuation Correction. *IEEE Transactions on Nuclear Science* **60,** 3391–3398. ISSN: 0018-9499 (Oct. 2013).

16. *3D Slicer* <http://www.slicer.org/> (2015).

17. Fedorov, A. *et al.* 3D Slicer as an image computing platform for the Quantitative Imaging Network. *Magnetic Resonance Imaging. Quantitative Imaging in Cancer* **30,** 1323–1341. ISSN: 0730-725X (Nov. 2012).

Publishing Agreement

It is the policy of the University to encourage the distribution of all theses, dissertations, and manuscripts. Copies of all UCSF theses, dissertations, and manuscripts will be routed to the library via the Graduate Division. The library will make all theses, dissertations, and manuscripts accessible to the public and will preserve these to the best of their abilities, in perpetuity.

Please sign the following statement:

I hereby grant permission to the Graduate Division of the University of California, San Francisco to release copies of my thesis, dissertation, or manuscript to the Campus Library to provide access and preservation, in whole or in part, in perpetuity.

_____   *Sept. 8, 2015*
Author Signature   Date